



Crystalline α -Sm₂S₃ nanowires: Structure and optical properties of an unusual intrinsically degenerate semiconductor

Chris M. Marin ^a, Lu Wang ^b, Joseph R. Brewer ^a, Wai-Ning Mei ^b, Chin Li Cheung ^{a,c,*}

^a Department of Chemistry, University of Nebraska-Lincoln, Lincoln, NE 68588, United States

^b Department of Physics, University of Nebraska at Omaha, Omaha, NE 68182, United States

^c Nebraska Center for Materials and Nanoscience, Lincoln, NE 68588, United States

ARTICLE INFO

Article history:

Received 1 November 2012

Received in revised form 11 February 2013

Accepted 13 February 2013

Available online 26 February 2013

Keywords:

Semiconductors

Rare earth compounds

Nanofabrication

Computer simulations

Vapor deposition

Electronic band structure

ABSTRACT

The lanthanide sulfides have long been a promising class of semiconductors because of their infrared-to-visible range band gaps and excellent thermoelectric properties. However, their applications have been limited due to their time consuming conventional synthetic processes and the lack of sufficient understanding of their electronic properties. To address these shortcomings, here we report a rapid, chemical vapor deposition route which results in thin films of crystalline α -phase samarium sesquisulfide (α -Sm₂S₃) nanowires within a few hours, rather than the typical 4–7 days required in previous synthetic processes. In addition, density functional theory was, for the first time, utilized to calculate the electronic band structure of α -Sm₂S₃ in order to shed insight into the interpretation of their UV-Vis absorption spectrum. We found that the theoretical direct gap in the band states of α -Sm₂S₃ is 1.7 eV. Computation results suggest that this gap can be tuned to a solar optimal ~1.3 eV via systematic sulfur vacancy sites engineered into the crystal structure. Most significantly, the degenerate semiconductor-like behavior long observed in lanthanide sulfide samples have been shown to be present even in the ideal α -Sm₂S₃ structure, suggesting that the observed heavily *p*-type behavior is an unusual intrinsic property of the material resulting from the Fermi level being located significantly below the optically active 1.7 eV band edge.

© 2013 Elsevier B.V. All rights reserved.

1. Introduction

The lanthanide sulfides are an intriguing class of semiconducting materials that are of considerable interest for their potential as high temperature thermoelectric materials [1], solar energy conversion materials [2], pigments [3], infrared window materials [4], and phosphor host media [5]. These applications largely stem from their visible light range absorption edges which provide the lanthanide series with their wide range of vibrant colors, from bright yellow (Yb₂S₃), to maroon (Ce₂S₃), to deep brown (Nd₂S₃) [6–8]. Despite their promise in displacing the use of toxic [9] cadmium chalcogenides in pigment applications [3], the lanthanide sulfides have not been utilized in many of the other cadmium chalcogenides' applications such as photovoltaics [10,11] and

quantum dots [12,13]. This can be attributed to the time- and energy-intensive conventional synthetic methods and, in part, to the unresolved nature of their optical absorption bands.

The lanthanide sulfides are typically synthesized by sulfurizing the corresponding lanthanide oxides [6–8,14,15] using the highly toxic sulfurization agent hydrogen sulfide (H₂S). Their reaction temperatures range from 1000 °C to 1200 °C with the actual process temperature depending on the lanthanide involved and the resulting crystal structure desired [7]. The major problem associated with this synthetic strategy is the long reaction time required to fully displace the oxygen from the starting oxide reactants: 4–7 days at the peak reaction temperature [6]. Recently, carbon disulfide (CS₂) had been applied as the sulfurization agent in place of H₂S [8]. CS₂ was found to be a more rapid sulfurization agent, bringing the sulfurization time down to around 3 h and the required sulfurization temperatures down to 800–1200 °C [8]. However, this superior sulfurization performance of CS₂ comes at the cost of a 1–5 at.% carbon incorporation into the resulting lanthanide sulfides [16].

In general, the lanthanides prefer to have +3 oxidation states, meaning that a sesquisulfide form (Ln₂S₃) is the preferred stoichiometry. Notably, Yb [6] and Sm [17] may also attain the +2 state,

Abbreviations: CVD, chemical vapor deposition; DFT, density functional theory; PDOSs, projected density of states; SAED, selected area electron diffraction; HRTEM, high resolution transmission electron microscopy; EDX, energy dispersive X-ray spectroscopy.

* Corresponding author. Address: 514A Hamilton Hall, University of Nebraska-Lincoln, Lincoln, NE 68588, United States. Tel.: +1 402 472 5172; fax: +1 402 472 9402.

E-mail address: ccheung2@unl.edu (C.L. Cheung).

but the +3 state is generally favored. The crystal structures of Ln_2S_3 generally can take one of four polymorphs: α , γ , δ , or ε . Originally, a β -phase had also been reported, but it has since been discarded because a slight amount of oxygen was later found to be required for its formation [18]. Between the fifteen lanthanide elements and four polymorphs, the resulting lanthanide sesquisulfide's absorption band edges can range from 1.56 eV (for γ phase Gd_2S_3) to 2.73 eV (for α phase La_2S_3) [7].

Beyond the rough absorption edges, little is known about the nature of the semiconducting band gaps involved with the lanthanide sulfides. This is largely due to the dramatic tailing edge (weak absorption occurring before the main absorption onset) observed in the experimental absorption spectra as noted by Glurdzhidze et al. as far back as 1979 [19]. Typically, this band tailing is considered indicative of a small concentration of impurities in the sample [20]. While Tauc plot analyses of various lanthanide sulfides were attempted as early as 1983 [6], the optical spectra of these semiconductors routinely failed to fit well with direct, indirect, or even direct and indirect forbidden models. Indeed, in a more recent study on single crystalline Gd_2S_3 and Ce_2S_3 samples, Witz et al. [21] could only postulate that some extrinsic sample effects were obfuscating their reflectivity and absorption data. Consequently, they recommended reliable band structure calculations in order to aid with interpreting these compounds' complex optical spectra.

Of the lanthanide sulfides, the samarium sulfide systems are of particular interest for their semiconductor applications. Since samarium exhibits a propensity for taking on both +2 and +3 oxidation states, the reported band gaps for the samarium sulfides range from 0.15 eV for SmS [22], to 2.18 eV for the γ -phase of Sm_2S_3 [7]. Among the different phases of samarium sulfides, α -phase Sm_2S_3 attracts an increasing amount of attention [23] due to its reported band gap in the infrared-to-red range, which are comparable to the industrially important cadmium selenide [12,24]. Nonetheless, challenges in understanding the electronic structures of $\alpha\text{-Sm}_2\text{S}_3$ have severely limited its industrial applications. Specifically, failures in applying the semiconductor models, used for simple p - and d -block compounds, to explain the reported absorption and reflectance spectra of Ln_2S_3 and their band tailing have led to speculations of impure samples in the reported literature and doubts as to the nature of its band gap. Moreover, the wide range of reported $\alpha\text{-Sm}_2\text{S}_3$'s absorption band edge values, from 1.69 eV [7] to 1.88 eV [8] and to even as high as 4.02 eV [23], has of yet been unresolved. The study of $\alpha\text{-Sm}_2\text{S}_3$ has further been exacerbated by the lack of reliable band structure calculations for the electron-dense f -block lanthanide sulfides.

Here we report a rapid synthesis of crystalline α -phase Sm_2S_3 by chemical vapor deposition and the characterization of its electronic structure via a combined approach of absorption spectroscopy and first principles calculations. Interestingly, these materials were found to have a high inherent tendency to crystallize as high aspect ratio nanowires with morphologies similar to naturally occurring amphiboles. Absorption spectroscopy of the resulting nanostructured films was taken both to characterize the rough band edge and band gap characteristics. In order to better understand the unexplained band tailing present in the absorption spectra of these materials, first principles density functional theory (DFT) calculations of ideal, Sm-deficient and S-deficient $\alpha\text{-Sm}_2\text{S}_3$ models were applied to compute possible electronic structures of $\alpha\text{-Sm}_2\text{S}_3$. Remarkably, our DFT study reveals that even in an ideal crystalline state, $\alpha\text{-Sm}_2\text{S}_3$ behaves as a heavily degenerate semiconductor (i.e. this material is intrinsically degenerate). This finding matches well with the peculiar experimentally observed behavior of these materials, providing explanation, for the first time, for the prominent tailing edges in their optical absorption spectra which have long been reported for these lanthanide sulfide systems.

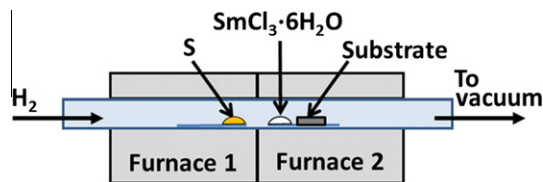


Fig. 1. Schematic of the experimental setup for the synthesis of $\alpha\text{-Sm}_2\text{S}_3$ nanowire films.

2. Materials and methods

The $\alpha\text{-Sm}_2\text{S}_3$ nanowire samples were synthesized by a CVD process in a 1-in. diameter quartz tube, inside a dual-furnace reactor. Samarium (III) chloride hexahydrate ($\text{SmCl}_3\cdot 6\text{H}_2\text{O}$), elemental sulfur (S), and hydrogen (H_2) were used as the chemical precursors (Fig. 1). The overall empirical reaction equation is proposed as: $2\text{SmCl}_3\cdot 6\text{H}_2\text{O}(\text{g}) + 3\text{S}(\text{g}) + 3\text{H}_2(\text{g}) \rightarrow \alpha\text{-Sm}_2\text{S}_3(\text{s}) + 6\text{HCl}(\text{g}) + 6\text{H}_2\text{O}(\text{g})$. $1 \times 1\text{-cm}^2$ (100) silicon wafers coated with 200-nm thick silicon nitride (University Wafer, South Boston, MA) and $1 \times 1\text{-cm}^2$ quartz slides were used as the substrates to collect products deposited during the reaction. The silicon nitride coating acted as a diffusion barrier to minimize the formation of silicides on the silicon chips during the reaction. Each substrate was pre-rinsed with ethanol and 18-MΩ de-ionized water, followed by drying with nitrogen before use. The silicon nitride coated substrate was located at 12 cm to the left of the center of the dual furnace. If a quartz substrate was to be coated to collect reaction products for their optical characterization, it was placed adjacent to the silicon nitride coated silicon chip.

In a typical reaction run, 0.1 g of elemental sulfur and 0.3 g of samarium (III) chloride hexahydrate (Sigma-Aldrich, Milwaukee, WI) were loaded on two separate quartz boats at 14 cm to the right of the center of Furnace 1 and at 13.5 cm to the left of the center of Furnace 2, respectively (Fig. 1). After the reactor system was pumped down to a base pressure below 9 m Torr, 100 standard cubic centimeters per minute (SCCM) of hydrogen (H_2) was applied to purge the quartz tube in the reactor system. Furnace 1 was then heated to 100 °C over a period of 20 min to vaporize the sulfur and to start the diffusion of sulfur throughout the system. Simultaneously, Furnace 2 was heated to 400 °C to remove the water from the samarium precursor. The flow of the H_2 carrier gas was stopped before Furnace 1 reached 35 °C. After Furnace 1 reached 100 °C and Furnace 2 reached 400 °C, their temperatures were held constant for 10 min until the reactor pressure re-stabilized. This was then followed by increasing the temperature of Furnace 2 to 875 °C and that of Furnace 1 to 200 °C over a period of 10 min. Afterwards, H_2 was re-added to the reaction at 100 SCCM for another 10 min. The typical reaction pressure was at ca. 0.6 Torr. At the end of the reaction, the flow of H_2 was stopped. Furnace 1 was opened fully to cool while Furnace 2 was cooled at a rate of over 5 °C/s down to 400 °C before being opened fully for cooling to room temperature.

The morphology and atomic lattice structures of the as-synthesized samples were characterized by field emission scanning electron microscopy (FESEM, Hitachi S-4700, Pleasanton, CA), X-ray powder diffraction (XRD) using a Rigaku D/Max-B Diffractometer (2 kW Cu K α X-ray beam with an average wavelength of 1.544 Å, Rigaku Americas, Woodlands, TX), and transmission electron microscopy (Tecnai F-20, FEI, Hillsboro, OR) with energy dispersive X-ray spectroscopy (EDX). TEM samples were prepared by sonicating the sulfide coated substrates in ethanol for 1–10 s until the ethanol became slightly cloudy, and then drop-casting this solution onto holey carbon TEM grids. UV-Vis-mid-IR absorption spectroscopy was performed on the sulfide coated quartz substrate and evaluated in comparison to a reference quartz standard using a Cary 5000 grating spectrophotometer (Agilent Technologies, Santa Clara, CA). Note that the use of absorption spectroscopy was necessary because the as-synthesized films were determined to be too thin for meaningful diffuse reflectance measurements.

3. Theory and calculations

Absorption spectrum analysis was performed using the standard Tauc method [25–29]. The model behind this method assumes that band-to-band transitions occur between a concave up and a concave down parabolic band in which the lower band is fully occupied and curved concave down. In such a case, it can be shown [20] that:

$$\alpha \cdot h\nu \propto (h\nu - E_g)^n \quad (1)$$

where α is the coefficient of absorption of the material, $h\nu$ is the energy of the incident photon, and E_g is the energy of the band gap being investigated. Additionally, the value of the exponential n provides insights into the relative positions of the two parabolic bands, where a value of $n = 1/2$ corresponds to a direct peak to valley

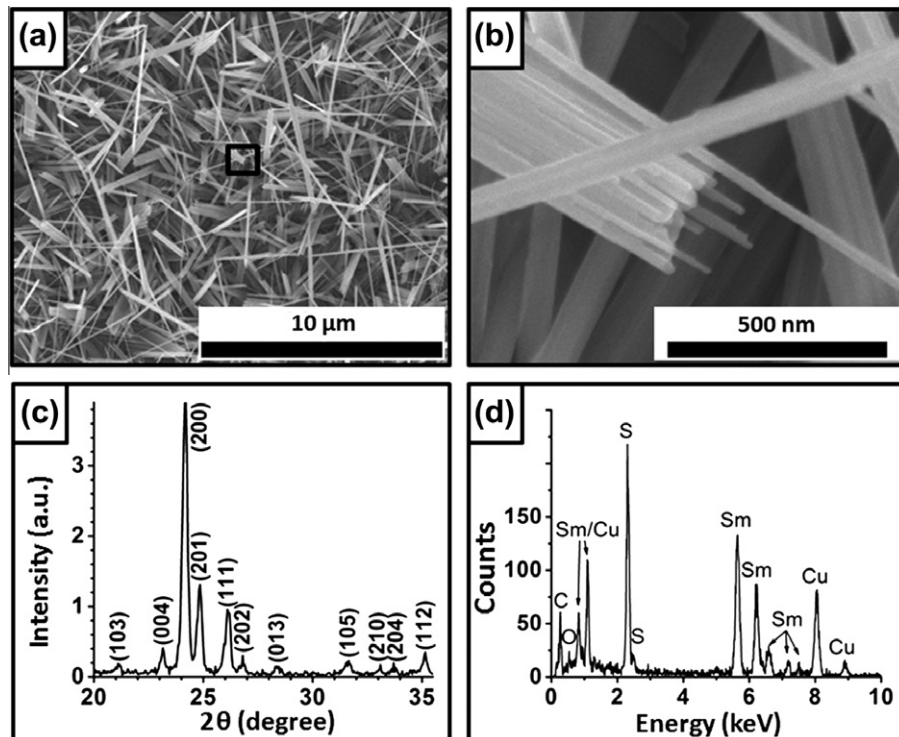


Fig. 2. (a) Representative SEM image of α -Sm₂S₃ nanowire film on a silicon nitride coated silicon chip. (b) Zoom-in image of the boxed area in Fig. 2a. The imaged wire bundling illustrates the typical morphology of wires produced in this system. (c) Typical XRD pattern of α -Sm₂S₃ nanostructured films. (d) EDX spectrum of α -Sm₂S₃ nanowires deposited on a holey carbon TEM grid.

transition between parabolic bands and a value of $n = 2$ corresponds to an indirect transition in which the peak of the valence band is not aligned in k space with valley of the conduction band. Under the assumptions used for Eq. (1), a Tauc plot, featuring $(\text{absorbance}-hv)^{1/n}$ on the y -axis plotted against photon energy on the x -axis, can be prepared. In such a plot, the value of n which results in a linear graph indicates the nature (direct, indirect, etc.) of the band gap, and the value of the extrapolated x -axis intercept of the linear plot provides the value of E_g .

On the computational side, density functional theory (DFT) implemented in the CASTEP code [30] was applied to calculate the band diagram and density of states of ideal, samarium-deficient, and sulfur-deficient α -Sm₂S₃ lattice models. The unit cell of ideal α -Sm₂S₃ is orthorhombic with space group Pnma (#62) symmetry and lattice parameters $a = 7.38 \text{ \AA}$, $b = 3.97 \text{ \AA}$, and $c = 15.36 \text{ \AA}$ containing 8 Sm and 12 S atoms. The plane wave basis set, with an energy cutoff of 380 eV ultra-soft pseudopotential, was employed together with the generalized gradient approximation (GGA), and Perdew–Burke–Ernzerhof (PBE) exchange and correlation functional [31]. The DFT + U method was used for the corrections of on-site coulomb interactions with $U = 6 \text{ eV}$ for Sm. In addition, we utilized the ensemble density functional theory (EDFT) [32,33] scheme programmed in CASTEP to overcome the convergence problem inherent in f -electron systems. Furthermore, we constructed two additional models with supercells double the size of the single unit cell (shown in Fig. 4a and b): one with an S vacancy site (i.e. 16 Sm atoms and 23 S atoms), and the other with a Sm vacancy site (i.e. 15 Sm atoms and 24 S atoms). This was done in order to simulate the effects of Sm-deficiency and S-deficiency on the band structure.

4. Results and discussion

Typically, the as-synthesized samarium sulfide samples appear as brownish “felt-like” textured films. FESEM reveals that these

films are composed of high aspect ratio wires that often bundle together to form cables of a wide variety of thicknesses and lengths of up to 15 μm (Fig. 2a and b). Individual wires generally have diameters of 15–30 nm. The product is identified as the alpha phase (orthorhombic) samarium sesquisulfide (α -Sm₂S₃) by matching the XRD patterns of these wire-textured films to the ICDD data (card # 04-007-4140) (Fig. 2c). While the peak positions in these patterns are strongly indicative of α -Sm₂S₃, the relative intensities of the various indexed peaks vary considerably from sample to sample, indicating a variety of preferred growth alignments. Nonetheless, these diffraction patterns do not appear to show any meaningful amount of samarium oxysulfide contamination. The EDX spectrum of the product obtained under TEM suggests the presence of mainly sulfur and samarium in these wires (Fig. 2d). The weak peaks in the spectrum indicating the presence of carbon, copper, and oxygen likely originate from the TEM grid.

High resolution TEM (HRTEM) characterization of the as-synthesized samples provided further insights into the short order crystal structure of the Sm₂S₃ nanowires (Fig. 3). Under the TEM, these wires were often terminated by flat or nearly flat ends and were generally found aggregated in a bundle form. Fig. 3a shows a wire bundle containing more than six obvious wires, each of which has a diameter of about 20 nm. Selected area electron diffraction (SAED) obtained at this bundle is complex due to the beam passing through multiple crystal grains (Fig. 3b). Interestingly, diffraction patterns of these bundles often indicate that the crystalline structures of these multiple grains share a common [010] orientation along the length of the wires.

Occasionally, isolated nanowires could be found on the TEM grid, allowing for an unobstructed study of the material's crystal structure. Fig. 3c shows the tip of an individual wire of ca. 60 nm in diameter with clearly visible vertical grain boundaries. While the very tip of the wire appears polycrystalline, the nanobeam SAED pattern obtained at the highlighted region (Fig. 3d) illustrates a much cleaner diffraction pattern than one which could be

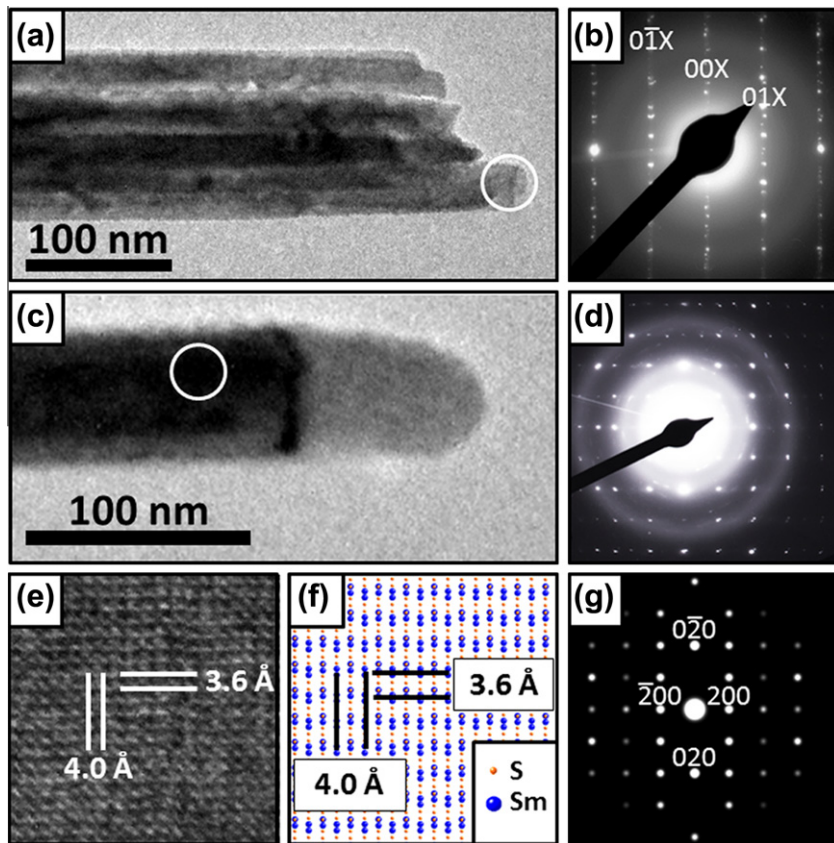


Fig. 3. (a) TEM image of a typical α - Sm_2S_3 wire bundle. The bundle has a width of 115 nm with an individual wire width of approximately 18 nm. (b) SAED of shown wire bundle taken at the location circled in (a). The parallel lines of the displayed diffraction spots suggest that one axis of orientation is shared amongst the different individual wires in the bundle. (c) TEM image of a separated individual wire. The change in darkness is due to phase contrast and a vertical grain boundary at the tip. (d) SAED of the individual wire at the circled location shown in (c). (e) HRTEM image of the wire shown in (c). (f) Extended CrystalMaker® crystal structure from the [001] view direction. (g) Simulated SAED spectra based on the crystal orientation indicated in (f). Note that this pattern matches well the diffraction spots in the lower right of (d), but this simulated pattern does not account for the weak spots in between strong spots shown on the left of (d).

obtained from a wire bundle (Fig. 3b). High resolution imaging of this region shows atomic lattice columns (Fig. 3e). This columnar alignment of atomic lattices is particularly significant since the α -phase lanthanide sesquisulfide crystal structure can only be tilted to show aligned columns when imaged in the [001] or [010] view direction. The simulated [001] view of the α - Sm_2S_3 lattice structure (Fig. 3f) generated using the CrystalMaker® software (Oxford, United Kingdom) matches well with the separation spacing among the lattice fringes in our HRTEM zoom-in image (Fig. 3e). Similar lattice matching models cannot be obtained in the case of the [010] view. This finding supports the [010] nanowire growth direction as indicated in Fig. 3b for the nanowire bundles. The corresponding simulated diffraction pattern in the [001] direction (Fig. 3g) also matches closely with the actual SAED pattern (Fig. 3d) taken at the circled area shown in Fig. 3c. Nonetheless, the left side of Fig. 3d shows what should be forbidden diffraction spots appear halfway in between the predicted diffraction spot positions (Fig. 3g). This likely implies a small break in the crystal symmetry of the sample, permitting otherwise forbidden peaks to appear under the right conditions.

To examine the origins of the experimental diffraction spots not explainable with our simulated SAED pattern for an ideal α - Sm_2S_3 lattice, we deliberately introduced either a samarium or sulfur atomic vacancy site in the ideal α - Sm_2S_3 crystal structure model and simulated the resulting SAED patterns (Fig. 4). The removal of either a sulfur atom (Fig. 4a, c, and e) or a samarium atom (Fig. 4b, d, and f) for every two unit cells resulted in almost identical diffraction patterns which showed weak diffraction spots

occurred halfway between each of the spots permitted by the ideal α - Sm_2S_3 crystal structure. Though the removal of one atom for every forty atoms in a dual-unit cell only constitutes a 2.5% atomic deficiency, such a modification introduces a break in the symmetry and hence causes these normally forbidden diffraction spots to arise. These normally forbidden diffraction spots resulting from the absence of a samarium atom were found to be more intense than those observed in the case of the sulfur atom absent model (Fig. 4d versus c). Our results can be possibly rationalized by noting that the influence of electron diffraction is larger for higher z atoms. Fig. 4e and f illustrates that the overlaid simulated SAED patterns fit that of the left side of the experimental diffraction pattern in Fig. 3d. This implies that a systematic atomic absence of sulfur or samarium is likely present in the region interrogated by part of the probing electron beam. Due to the difference in the intensity of some of the “forbidden” diffraction spots, we suspect that this sample is samarium deficient, at least in the illustrated section of this nanowire.

The optical absorption of the as-synthesized α - Sm_2S_3 nanowire film was evaluated via UV-Vis absorption spectroscopy to determine its band gap characteristics. The absorption band edge of the α - Sm_2S_3 nanowire film roughly coincides with the previously reported band edge, intercepting at about 700 nm (1.77 eV) [7] (Fig. 5a). Optical absorption of the film starts below 2200 nm (0.56 eV) with absorption gradually increasing towards shorter wavelengths. This band tailing phenomenon has been reported before among the absorption spectra of lanthanide sulfides [19,21]. The largest characteristic f -to- f transition absorption peaks of

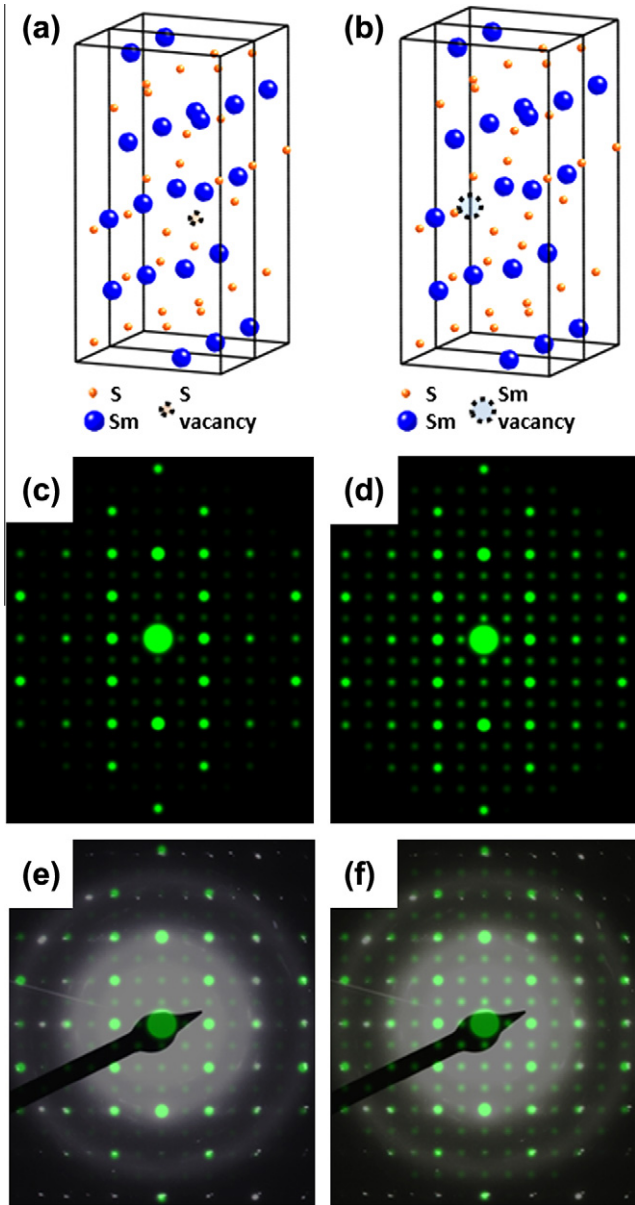


Fig. 4. Simulated models of α -Sm₂S₃: (a) model showing the systematic absence of a single sulfur atom for every two unit cells. (b) Model showing the absence of a single samarium atom for every two unit cells. (c) Simulated electron diffraction pattern for the model in (a). Note the presence of the faint spots between major spots. (d) Simulated electron diffraction pattern for model (b) under identical conditions as for (c). This pattern is similar to the one in (c) except that the weak spots between the major diffraction spots are relatively more intense. (e) Simulated diffraction pattern in (c) (green) overlaid on the data from Fig. 3d (white). All experimentally observed spots fall under either the normal intense spots, or the fainter spots attributed to the missing sulfur atoms in the unit cell. (f) Simulated diffraction pattern in (d) (green) overlaid on the data from Fig. 3d (white). The brighter in between spots better account for the experimental data. (For interpretation of the references to color in this figure legend, the reader is referred to the web version of this article.)

samarium sulfide remain observable at 1100, 1270, and 1410 nm, corresponding well to previously reported results for α -Sm₂S₃ [7]. To better assess the characteristics of the sample's band gap, we compare two Tauc plots using the absorption data, one assuming a direct band gap model (Eq. (1), $n = 1/2$) (Fig. 5b) and another assuming an indirect band gap model (Eq. (1), $n = 2$) [20] (Fig. 5c). If we assume that the synthesized α -Sm₂S₃ nanowire film has a direct band gap, an extrapolated straight line fit of the corresponding

Tauc plot would predict a direct band gap of ca. 2.4 eV (Fig. 5b). As shown in the absorption spectrum, the very large band tailing is once again very apparent in this plot. Indeed, this kind of trailing edge is typically indicative of dopant states present in a pure semiconductor [20]. In contrast, if we assume that the sample has an indirect band gap, the extrapolated line fit of the corresponding Tauc plot indicates the expected gap energy to be close to 0 eV (Fig. 5c).

First principles DFT calculations of the electronic structure of α -Sm₂S₃ reveal several interesting features in the calculated band structure. First, the Fermi level in α -Sm₂S₃ is observed to lie in the midst of a large number of bands (Fig. 6a). The corresponding projected density of states (PDOSs) diagram indicates that most of these bands are from the p -orbital contributions to the extended crystal structure (Fig. 6d). This would suggest that α -Sm₂S₃ is predicted to be metallic since right above the theoretical Fermi level E_F , there are a large number of permissible empty states spanning a width of 0.6 eV. However, above that there lies a direct 1.7 eV gap in the permissible band states rendering the total band gap to be 2.3 eV originally counting from E_F . These features are also visible in the experimental absorption spectrum (Fig. 5). In particular, the absorption spectrum manifests a sharp increase in absorption starting around 1.77 eV, verifying the 1.7 eV gap found in the DFT calculated band structure. Additionally, according to the Tauc analysis of the absorption data (Fig. 5b and c), the direct gap should be about 2.4 eV, a tight fit to the 2.3 eV found by the DFT calculations, while the indirect gap is found to be near 0 eV, which the DFT calculations do show to be an allowed transition. Hence the data implies that the α -Sm₂S₃ may turn out to be an unconventional kind of p -type semiconductor with an abundant density of holes near E_F . In fact, similar observations on FeS₂ were reported by Sun et al. [34]. However, in the case of FeS₂, Sun et al. ascribed this

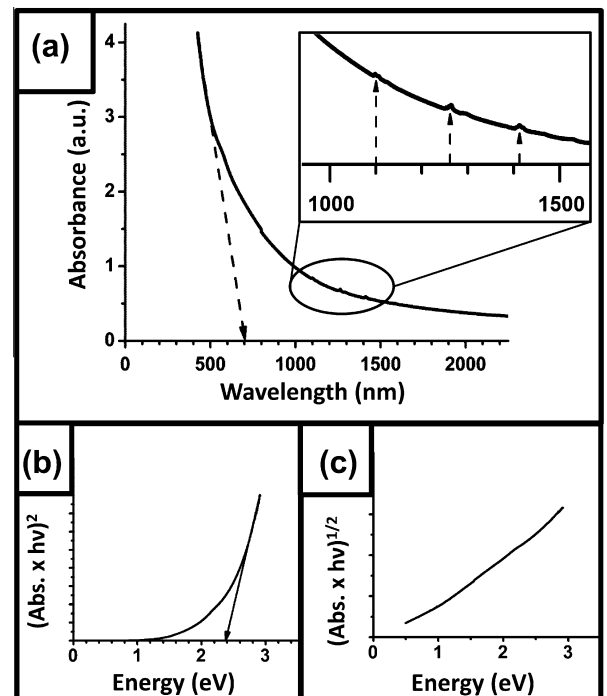


Fig. 5. (a) Absorption spectrum of a α -Sm₂S₃ nanowire film with the arrow indicating the rough band edge at about 700 nm (1.77 eV) (inset). Magnified view of the circled region showing the characteristic f -to- f transition peaks of Sm₂S₃. Note: the small vertical line around 800 nm is an artifact due to the change-over of detectors. (b) Tauc plot of absorption data using a direct band gap model. The direct band gap was estimated to be 2.4 eV (arrow). (c) Tauc plot of absorption data using an indirect band gap model. The indirect band gap was estimated to be near 0 eV.

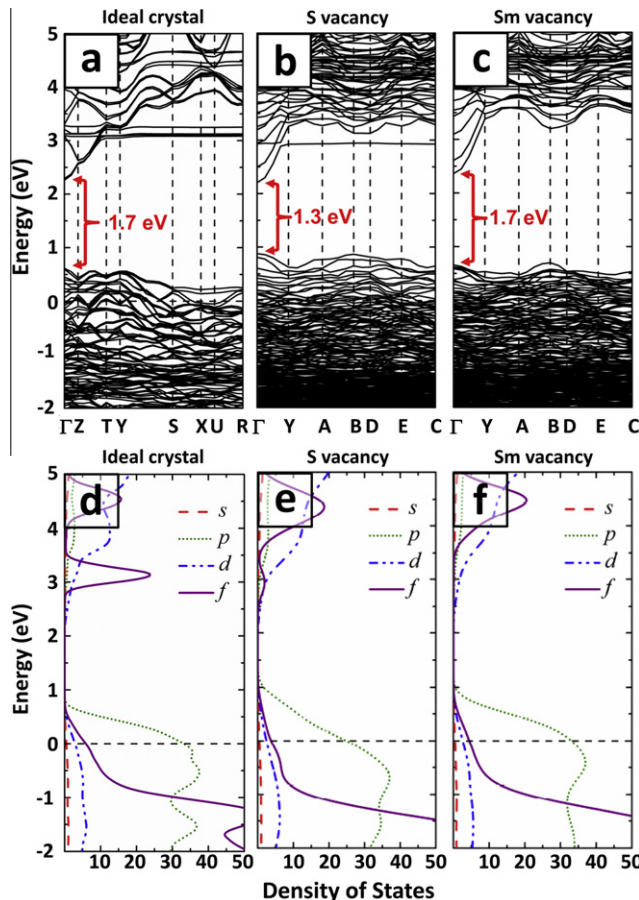


Fig. 6. Band diagrams for (a) ideal 2:3 stoichiometry single crystalline α - Sm_2S_3 , (b) sulfur-deficient $\text{Sm}_{2.875}\text{S}_3$, and (c) samarium-deficient $\text{Sm}_{1.875}\text{S}_3$ derived from DFT calculations. Density of state diagrams for the stoichiometric, sulfur-deficient, and samarium-deficient models are displayed in (d), (e), and (f), respectively. The Fermi level is indicated by the dashed lines.

ubiquitous *p*-type conductivity to oxygen impurities. For Sm_2S_3 , this behavior appears to be truly intrinsic since there are expected to be a density of holes near the Fermi level even for the perfect unit cell used for DFT calculations.

Since our SAED studies of the α - Sm_2S_3 nanowires suggest that the crystal structure of our samples could have various systematic atomic vacancy sites, we performed additional DFT calculations to yield insights into the effects of such non-idealities on the electronic structure and band diagram of this material. Electronic structure computations were performed for the same models as indicated in Fig. 4a and b to explore the two cases where either a single sulfur or samarium atom is missing for every two α - Sm_2S_3 unit cells. Thus, these two case models have a 2.5% atomic deficiency. In these deficient models, we maintained the lattice parameters and optimized the atomic positions. The calculated band structures and the corresponding densities of states of these two models display some features similar to the case of the ideal structure, but also some distinct features (Fig. 6). As a point of similarity, the Fermi levels for both models with vacancy defects remain consistently placed in the lower bands. This implies that α - Sm_2S_3 with a slight atomic deficiency (2.5% of atoms missing) in either samarium or sulfur should still possess a *p*-type degenerate semiconductor resembling electronic structure. As a major point of difference, both atom-deficient structures display reductions in the occupancies of the *f*-shell electrons around 3 eV in their density of state diagrams. This is expected to lead to a reduction of observed *f*-to-*f* transitions in optical absorption measurements, suggesting that monitoring the intensity of the absorption spikes (Fig. 5 at

1100 nm, 1270 nm, and 1410 nm) may be a useful way of indicating sample purity. Finally, since the *p*-orbital electrons in particular overlap the Fermi level, it is worth pointing out that the sulfur-deficient model shows the biggest change in the density of states for the *p*-orbitals. For instance, in both the ideal crystal and the samarium-deficient crystal, the corresponding *p*-orbital PDOS's at the Fermi level remain steady at 33 electron state/eV. Yet, the sulfur-deficient system has a *p*-orbital PDOS of 25 electron state/eV. Nevertheless, the remaining *p*-states of this sulfur-deficient system are shifted upward due to the oxidation state changes of samarium, rendering the direct gap in the band states of this model to be reduced to 1.3 eV (Fig. 6b), which is an ideal band gap value in the functional solar cell range [35]. We further notice that the direct gap remains about the same, 1.7 eV, for the Sm-deficient model as compared to that of the ideal Sm_2S_3 (Fig. 6a and c). This suggests that careful control of the sulfur content in the unit cells may be particularly useful for controlling the degree of degeneracy and overall band gap of $\text{Sm}_{2-x}\text{S}_3$ systems.

5. Conclusion

In summary, α - Sm_2S_3 has been successfully synthesized via a new chemical vapor deposition based process which resulted in films composed of highly crystalline nanowires with a consistent [010] growth direction. The rough absorption edge of the α - Sm_2S_3 films produced by our method was found to be about 1.77 eV, a result that matches well with prior Sm_2S_3 studies [7,8]. Density functional theory calculations predict that an ideal α - Sm_2S_3 crystal should have a direct gap in the band states spanning 1.7 eV. However, due to the Fermi level being located 0.6 eV below the direct band gap, a full transition from the Fermi level to above the band gap requires 2.3 eV, a value that corroborates well with the 2.4 eV direct band gap value realized in the Tauc plot of the absorption data. Taken together, this data strongly suggests that α - Sm_2S_3 behaves intrinsically like a heavily doped *p*-type semiconductor, a property which has long been directly observed in the heavy band tailing in the absorption spectra of this class of materials [6–8,21,23]. This property may make α - Sm_2S_3 particularly well-suited for serving as the *p*-type leg of photovoltaic diodes or thermoelectric generators.

Our theoretical calculations illustrate that both samarium-deficient and sulfur-deficient crystal structures retain the distinct *p*-type degenerate-semiconductor-like band structures of the pure α - Sm_2S_3 , but with significant modifications in the PDOS occupancies of the *p*- and *f*-shells neighboring the band gap. This suggests an encouraging method for controlling the electronic properties of samarium sesquisulfide, such as reducing the direct gap in the band states to a theoretical solar optimal value of ~1.3 eV [35] by modulating the atomic vacancies. Since the large trailing edge exhibited at the lower photon energies of our α - Sm_2S_3 film's absorption spectrum frequently appears in absorption spectra of *f*-block systems [19,21], such fascinating "tailing" features in other lanthanide systems may likely be similarly rationalized using band extension arguments as in our theoretical electronic structure arguments for α - Sm_2S_3 . We expect that this intrinsically degenerate behavior may be ideal in situations which require the use of a semiconductor, but are not amenable to extrinsic doping. Additionally, the predicted tunability of Sm_2S_3 's optically active direct gap may make it an excellent candidate as a next generation photovoltaic material.

Author contributions

The manuscript was written through contributions and discussion among all authors. Cheung, Marin, and Brewer designed and

conducted the synthesis and the structure and optical characterization of the samarium sulfide materials. Wang and Mei executed the DFT calculation portion of the presented data. All authors approved the final article.

Notes

The authors declare no competing financial interest. Funding sources had no involvement in the data collection, analysis, or interpretation of the data disclosed in this article, nor in the decision to publish.

Acknowledgments

We thank funding support in part from the Maude Hammond Fling Faculty Research Fellowship, Nebraska Research Initiative, Nebraska Center for Energy Sciences, NSF-EPSCoR (EPS-1010674) and U.S. Department of Energy (DE-EE0003174). CMM is financially supported by the Department of Education GAAN fellowship (P200A100041). The University of Nebraska Holland Computing Center provided computations resources with the associated USCMS Tier-2 site at the University of Nebraska-Lincoln. We are grateful to Johnny Goodwin at the University of Alabama and David Diercks at the University of North Texas for their help with microscopy and Hsin-Yu Liu for his helpful discussions. We acknowledge the Center of Biotechnology and Nebraska Center for Materials and Nanoscience for the use of their materials characterization facilities.

References

- [1] A.V. Golubkov, M.M. Kazanin, V.V. Kaminskii, V.V. Sokolov, S.M. Solov'ev, L.N. Trushnikova, Inorg. Mater. 39 (2003) 1251–1256.
- [2] S.B. Jundale, C.D. Lokhande, Sol. Energy Mater. Sol. Cells 28 (1992) 151–157.
- [3] P. Maestro, D. Huguenin, J. Alloys Comp. 225 (1995) 520–528.
- [4] D.L. Chess, C.A. Chess, J.V. Biggers, W.B. White, J. Am. Ceram. Soc. 66 (1983) 18–22.
- [5] W.M. Yim, A.K. Fan, E.J. Stofko, J. Electrochem. Soc. 120 (1973) 441–446.
- [6] O. Schevciw, W.B. White, Mater. Res. Bull. 18 (1983) 1059–1068.
- [7] C.M. Forster, W.B. White, Mater. Res. Bull. 41 (2005) 448–454.
- [8] H. Yuan, J. Zhang, R. Yu, Q. Su, J. Rare Earths 27 (2009) 308–311.
- [9] R.K. Zalups, D.J. Koropatnick, Molecular Biology and Toxicology of Metals, Taylor & Francis, New York, 2000.
- [10] S.M. Reda, Acta Mater. 56 (2008) 259–264.
- [11] D. Bonnet, P. Meyers, J. Mater. Res. 13 (1998) 2740–2753.
- [12] M.A. van Huis, A. van Veen, H. Schut, S.W.H. Eijt, B.J. Kooi, J.Th.M. De Hosson, Acta Mater. 53 (2005) 1305–1311.
- [13] J.K. Jaiswal, S.M. Simon, Trends Cell Biol. 14 (2004) 497–504.
- [14] L. Havlak, V. Jary, M. Nikl, P. Bohacek, J. Barta, Acta Mater. 59 (2011) 6219–6227.
- [15] J. Flahaut, M. Guittard, M. Patrie, Bull. Soc. Chim. Fr. (1959) 1917–1920.
- [16] M. Ohta, H. Yuan, S. Hirai, Y. Yajima, T. Nishimura, K. Shimakage, J. Alloys Comp. 451 (2008) 627–631.
- [17] M. Picon, L. Domange, J. Flahaut, M. Guittard, M. Patrie, Bull. Soc. Chim. Fr. 2 (1960) 221–228.
- [18] C.M. Vaughan, W.B. White, MRS Proc. 97 (1987) 397–402.
- [19] L.N. Glurdzhidze, T.D. Kekhaiov, T.L. Bzhalava, Z.U. Dzhabua, V.V. Sanadze, Sov. Phys. Solid State 21 (1979) 2021–2023.
- [20] J.I. Pankove, Optical Processes in Semiconductors, Dover, New York, 1971.
- [21] C. Witz, D. Huguenin, J. Lafait, S. Dupont, M.L. Theye, J. Appl. Phys. 79 (1995) 2038–2042.
- [22] B. Batlogg, E. Kaldis, A. Schlegel, P. Wachter, Phys. Rev. B 14 (1976) 5503–5514.
- [23] Y.-C. Hou, J.-F. Huang, X. Zhou, L.-Y. Cao, L.-X. Yin, J. Alloys Comp. 536 (2012) 119–123.
- [24] U. Pal, D. Samanta, S. Ghorai, A.K. Chaudhuri, J. Appl. Phys. 74 (1993) 6368–6374.
- [25] S. Jeon, S.-E. Ahn, I. Song, C.J. Kim, U.-I. Chung, E. Lee, I. Yoo, A. Nathan, S. Lee, J. Robertson, K. Kim, Nature Mater. 11 (2012) 301–305.
- [26] A.M. Guloy, R. Ramlau, Z. Tang, W. Schnelle, M. Baitinger, Y. Grin, Nature 443 (2006) 320–323.
- [27] L.T. Liu, C. Kopas, R.K. Singh, R.M. Hanley, N. Newman, Thin Solid Films 520 (2012) 6153–6157.
- [28] K. Muthu, S.P. Meenakshisundaram, Mater. Lett. 84 (2012) 56–58.
- [29] J. Tauc, Mater. Res. Bull. 3 (1968) 37–46.
- [30] M.D. Segall, P.J.D. Lindan, M.J. Probert, C.J. Pickard, P.J. Hasnip, S.J. Clark, M.C. Payne, Phys. Condens. Matter 14 (2002) 2717–2744.
- [31] J.P. Perdew, K. Burke, M. Ernzerhof, Phys. Rev. Lett. 77 (1996) 3865–3868.
- [32] N. Marzari, D. Vanderbilt, M.C. Payne, Phys. Rev. Lett. 79 (1997) 1337–1340.
- [33] M.C. Payne, M.P. Teter, D.C. Allan, T.A. Arias, J.D. Joannopoulos, Rev. Mod. Phys. 64 (1992) 1045–1097.
- [34] R. Sun, M.K.Y. Chan, S.Y. Kang, G. Ceder, Phys. Rev. B 84 (2011) 035212.
- [35] G.L. Araujo, A. Marti, Sol. Energy Mater. Sol. Cells 33 (1994) 213–240.